Modeling Boundary-Layer Transition in Subsonic Flow over a Swept Wing

Ethan S. Beyak*, Meelan Choudhari†, and Fei Li‡
NASA Langley Research Center, Hampton, VA 23681, USA

Balaji Shankar Venkatachari§
Analytical Mechanical Associates Inc., Hampton, VA 23666, USA

Pedro Paredes¶
National Institute of Aerospace, Hampton, VA 23666, USA

Predicting the onset of boundary-layer transition is often more accurate using physics-based models that directly compute disturbance growth rather than phenomenological models often implemented into industrial CFD codes. The aim of this ongoing study is to calibrate linear, physics-based computations of transition in subsonic flows over swept wings against a large set of experimental data. Advancing the calibration of linear models of transition contributes to the CFD-Vision-2030 goal of automated boundary-layer transition prediction. This progress report uses the dual *N*-factor method to model transition over the swept NACA 64_2015A wing. The flow conditions match selected test conditions from an extensive experimental dataset acquired from the NASA Ames 12-ft Pressure Tunnel. The OVERFLOW 2.4b flow solver is used to obtain laminar basic states based on an infinite-span assumption. Stability analyses are performed on 365 distinct configurations with linear stability theory (LST) and parabolized stability equations (PSE) from the Langley Stability and Transition Analysis Codes (LASTRAC), modeling the growth of Tollmien-Schlichting (TS) and stationary crossflow (SCF) disturbances. From a total of 67 data points for unswept, i.e., TS-dominant configurations, the critical *N*-factor based on PSE is found to be $N_{\mathrm{TS}} \approx 9$. The SCF critical *N*-factor is found to be near 8 for the highly swept, SCF-dominant configurations. Dual *N*-factor curves for both LST and PSE computations demonstrate a high level of interaction between TS and SCF. It may be worthwhile to investigate an alternate metric to visualize maximal SCF amplification upstream of the transition location to account for the growth of SCF modes near the leading edge, which is not considered in the conventional applications of the dual *N*-factor criterion.

Nomenclature

C_p	=	Surface pressure coefficient, $(p_w - p_\infty)/(\frac{1}{2}\rho_\infty V_\infty^2)$ [nondimensional]
c	=	chord length, normal to the leading edge [m]
M_∞	=	Freestream Mach number [nondimensional]
N	=	N-factor (natural log of relative disturbance amplification) [nondimensional]
V_∞	=	Resultant freestream velocity [m/s]
Re_x	=	Reynolds number based on a selected x location, $\rho_\infty V_\infty x/\mu_\infty$ [nondimensional]
Re_c	=	Reynolds number based on chord, $\rho_\infty V_\infty c/\mu_\infty$ [nondimensional]
$\mathrm{Re}_{\mathrm{tr}}$	=	Reynolds number based on transition location, $\rho_\infty V_\infty x_{\mathrm{tr}}/\mu_\infty$ [nondimensional]
Re_θ	=	Reynolds number based on momentum thickness, $\rho_\infty V_\infty \theta/\mu_\infty$ [nondimensional]
s	=	Surface streamwise coordinate, $s = 0$ at the attachment line [m]
T	=	Temperature [K]

*Aerospace Technologist, ethan.s.beyak@nasa.gov, AIAA Member
†Aerospace Technologist, m.m.choudhari@nasa.gov, AIAA Fellow
‡Aerospace Technologist, fei.li@nasa.gov
§Sr. Research Scientist, balaji.s.venkatachari@nasa.gov, Senior AIAA Member
¶Associate Research Fellow, pedro.paredes@nasa.gov, AIAA Associate Fellow

u = Chordwise component of velocity [m/s]
w = Spanwise component of velocity [m/s]
x = Leading-edge-orthogonal chordwise coordinate [nondimensional]
x_{tr} = x-coordinate of transition as measured by experimental diagnostics [m]
y = Wall-normal coordinate [m]
y_c = Clustering height near boundary-layer edge, Eq. (4) [m]
$y_{\max}$ = Maximum y-coordinate [m]
z = Leading-edge-parallel coordinate, component-3 of the local frame [nondimensional]
ℓ = The local, similarity boundary-layer length scale, Eq. (5) [m]
α = Angle of attack [degrees]
α_r = Real part of the streamwise wavenumber of the disturbance [1/m]
α_i = Imaginary part of the streamwise wavenumber of the disturbance [1/m]
α_{ISW} = Angle of attack (local frame) for an infinite swept wing in free flight [degrees]
$\alpha_{\text{3D,WT}}$ = Angle of attack for a three-dimensional wing in a wind tunnel, Section II.B [degrees]
β = Disturbance spanwise wavenumber, $2\pi/\lambda_z$ [rad/m]
β_{ss} = Side-slip angle, Eq. (2) [degrees]
δ = Representative boundary-layer thickness [m]
λ_z = Spanwise component of disturbance wavelength [m]
Λ = Sweep angle [degrees]
μ_t = Eddy viscosity [kg m/s]
μ = Dynamic viscosity [kg m/s]
ν = Kinematic viscosity [m^2/s]
ρ = Mass density [kg/m^3]

Subscripts

crit = Critical quantity, i.e., associated with the transition onset location
e = Value of quantity at the end of the wall-normal domain
∞ = Freestream quantity
ISW = Infinite-swept-wing quantity
TS = Related to Tollmien-Schlichting waves
TS, crit = Critical quantity related to TS waves
SCF = Related to stationary crossflow
SCF, crit = Critical quantity related to SCF
w = Quantity value at the wall (surface)

Accents

$\hat{q}$ = Eigenvector or shape-function component
$\mathbf{q}$ = Vector quantity
$\overline{q}$ = Base-flow quantity

I. Introduction

Accurate prediction of laminar-to-turbulent boundary-layer transition is crucial for many modern problems in engineering and science. One problem of particular importance in aerospace engineering is combating the climate crisis. Aviation's impact can be mitigated by reducing fuel burn which is directly related to reducing the vehicle drag. There are three important facts to note: a) about 1/2 of the total drag of commercial transport aircraft corresponds to skin-friction drag [1], b) laminar skin friction is nearly an order of magnitude lower than turbulent skin friction at an equivalent Reynolds number [2], and c) wing profile drag for an average transport aircraft is dominated by skin-friction drag and accounts for 1/3 of the total drag of the aircraft [3]. With these in mind, if the boundary layer remains laminar over a large extent of the wings, then there will be a significant increase in the overall energy efficiency of the aircraft, ultimately reducing aviation's contribution to the climate crisis.

The physics of boundary-layer transition is inherently nonlinear, as it is dependent upon finite amplitude disturbances. As external disturbances from the freestream interact with the boundary layer, they excite instabilities that amplify exponentially over a large distance. Ultimately, these instabilities break down the laminar boundary layer through a sequence of nonlinear interactions [4], and soon downstream, the boundary layer reaches a fully turbulent state.

Despite this nonlinear physics, it is common for transition prediction to focus solely on the exponential growth of the disturbance amplitude because it can be modeled by linear computations asserting infinitesimal disturbance amplitudes. In practice, this stage of the transition process tends to be the largest region for a number of flow configurations, i.e., the receptivity and transition-zone lengths are generally shorter. Thus, if the linear dynamics of the disturbances are characterized accurately, then reasonable approximations can be made regarding the entirety of the laminar-to-turbulent transition process. This is a common approach in literature with regard to transition over a subsonic, swept wing [5–10].

Many, if not most, CFD computations at industrial scales do not physically model the disturbance growth in the transition process. Instead, flow may be assumed turbulent from the attachment line, which permits the use of Reynolds-averaged Navier-Stokes (RANS)-based turbulence models throughout the flowfield. These are computationally efficient, but are inappropriate if laminar flow ought to be physically modeled. Additionally, the boundary layer may be numerically tripped at a specified location downstream, or transition may be modeled using auxiliary, transport partial differential equations, e.g., the Langtry-Menter model [11].

The geometry of the present work is an untapered swept wing. Two relevant primary instability mechanisms are the Tollmien-Schlichting (TS) instability and the stationary crossflow (SCF) instability. Generally, TS-based transition on swept wings is well predicted with a suitably calibrated N-factor correlation, as well as transport-equation-based models such as the Langtry model (see Leidy et al. [12] as a demonstration). However, crossflow development is presently not as well predicted by transport-based models, and crossflow transition is highly sensitive to both surface roughness and freestream turbulence. Those dependencies are not fully understood due to the small number of benchmark-quality experimental datasets and/or accompanying analysis. Furthermore, crossflow amplification is also influenced by nonparallel effects as well as the surface curvature. Reduced-order physics-based models, such as the e^N-method, can be effective at transition prediction when the boundary layer has one dominant instability mechanism. However, in the presence of multiple instability mechanisms undergoing appreciable growth, the e^N-method does not account for mixed-mode interactions. In these scenarios, the dual N-factor method can be adopted to approximate the mixed-mode interaction through linear amplification levels. However, the database of dual N-factor computations including basic-state nonparallelism is rather limited. The goal of this ongoing effort is to address that limitation with stability analyses for an extensive set of measurements over an untapered swept wing. An additional goal is to quantify the variation in dual N-factor correlations across different facilities (albeit with relatively low levels of freestream turbulence) and different test models (with similar levels of surface finish). These goals are consistent with those outlined in the CFD Vision 2030 [13]. With the CFD practitioner's perspective in mind, this work will improve CFD's capability for transition prediction in subsonic, swept-wing flows. The extensive database of swept-wing transition measurements by Boltz et al. [14] is used in this paper to assess the stability-based transition modeling with a coupled analysis involving the LASTRAC instability analysis solver and the OVERFLOW CFD solver.

The manuscript is organized as follows. Section II provides an overview of the experimental setup from Boltz et al. [14] and the computational methodology. Section III presents selected results regarding base-flow convergence, comparison with other results from the literature, and stability analysis of Tollmien-Schlichting and stationary crossflow disturbances. Finally, Section IV presents a summary of the work completed thus far and outlines follow-on analysis.

II. Methodology

A. Overview of Experimental Setup

Experimental measurements of transition locations on the upper surface of the NACA 64_2015A wing are given by Boltz et al. [14]. These measurements were conducted in the NASA Ames 12-Foot Low-Turbulence Pressure Tunnel at a freestream Mach number of 0.27. In the paper by Boltz et al., Figure 1 shows that the wing can be swept so that the leading edge could attain sweep angles of 0°, 10°, 20°, 30°, 40°, and 50° with replacement leading and trailing edges at the root. Various wingtips were also available, but each leading-edge sweep angle was obtained by making a physical model change. The angle of attack was accomplished by a simple change in the turntable and could be adjusted during each run while the tunnel is running. The semi-span model is mounted on one wall, giving rise to both wall effects and 3D geometrical effects. The freestream Reynolds number was varied by changing the tunnel speed at each α and Λ to cause transition onset near specific chordwise stations ($x_{\text{tr}}/c \in [0.21, 0.24, 0.30, 0.35, 0.40, 0.45]$). Small microphones

were installed on the wing surface and the Reynolds number was varied until an aural and visual assessment determined that the surface pressure signal at the microphone location of interest had evolved into a transitional state.

The chord of the wing is 4 ft (1.2192 m). The angle of attack range at $\Lambda = 0°$ was $\alpha \in [-3°, +4°]$, $\Delta\alpha = 0.5°$, whereas for nonzero sweep angles $[10°, 20°, 30°, 40°, 50°]$, it was restricted to $\alpha \in [-3°, +3°]$. Thus, the configurations tested by Boltz et al. [14] span over 6 different sweep angles, 13 angles of attack (15 for $\Lambda = 0°$), and for this work, there are on average about 5 different x_{tr}/c locations for each geometric configuration*. This leads to about 400 distinct experimental configurations, all succinctly summarized in Figures 7 and 9 of Boltz et al. [14], from which the freestream Reynolds numbers are extracted.

Having described the flow configurations of interest, we next discuss the computational process for basic-state generation, definitions of coordinate systems, and the relevant geometric angles.

B. Overview of Basic-State Computations

For the purpose of basic-state computations for stability analysis, we restrict our attention to fully attached flows and assume the effects of viscous-inviscid interaction to be sufficiently small so that the computed laminar profiles are not very sensitive to the imposed transition location. However, if necessary, the codes employed herein also allow a fully coupled, iterative computation as demonstrated in previous works [15–17]. To allow basic-state computations all the way up to the measured transition location, and to shield the laminar region from upstream effects of the boundary-layer "tripping," we perform a single basic-state computation for each flow condition that imposes transition at $x/c \approx 0.45$, slightly downstream of the onset of an adverse pressure gradient starting near $x/c = 0.40$ for many configurations†. The solutions are tripped turbulent to avoid unsteady laminar separation bubbles on the aft portion of the wing.

We now describe the frames of reference and geometric angles used in this manuscript. In the global, wind-tunnel frame denoted with a subscript g, the axes are 1) down the tunnel, 2) upward against gravity, and 3) sideways to complete the right-hand rule. The freestream velocity vector has one downstream component: $\mathbf{V}_{\infty,g} = [V_\infty, 0, 0]$ (assuming there is no helical flow in the freestream). Rotating by the angle of attack in this frame about the 3-axis gives $\mathbf{V}_{\infty,A} = [V_\infty \cos(\alpha_A), V_\infty \sin(\alpha_A), 0]$, defining α_A and the frame A. This angle of attack can be labeled as the three-dimensional, wind-tunnel angle of attack: $\alpha_{3D,WT} \equiv \alpha_A$. Rotating by $-\Lambda$ in this frame about the 2-axis gives $\mathbf{V}_{\infty,B} = [u_\infty, v_\infty, w_\infty] = [V_\infty \cos(\alpha_{3D,WT}) \cos(\Lambda), V_\infty \sin(\alpha_{3D,WT}), V_\infty \cos(\alpha_{3D,WT}) \sin(\Lambda)]$, defining the frame B. In this B frame, the 3-axis is now aligned with the sweep of the wing, i.e., leading-edge-parallel and is labeled as z. The 1-axis in this frame is aligned with the leading-edge-orthogonal direction from the leading edge to the trailing edge, which we label as x. Because of this, the B frame can also be referred to as the local frame.

It is advantageous to derive the relation for the angle of attack in the local, cross-section frame, which is done by considering the ratio of v_∞ and u_∞. This angle of attack in the local frame (B) is denoted as α_B, indicating a rotation about quarter-chord, and is computed through

$$\tan(\alpha_B) = \frac{v_\infty}{u_\infty} = \frac{V_\infty \sin(\alpha_{3D,WT})}{V_\infty \cos(\alpha_{3D,WT}) \cos(\Lambda)} = \frac{\tan(\alpha_{3D,WT})}{\cos(\Lambda)}. \tag{1}$$

Note that Eq. (1) can be compared to Eq. 3 in Franciolini et al. [19]. The side-slip angle is computed through

$$\sin(\beta_{ss}) = \frac{w_\infty}{\sqrt{u_\infty^2 + v_\infty^2 + w_\infty^2}} = \cos(\alpha_{3D,WT}) \sin(\Lambda) \tag{2}$$

after some algebraic manipulation.

In the pursuit of computational efficiency, the wind tunnel is not included in the computational mesh. Instead, the flow over the wing is modeled as spanwise infinite. Since there is blockage in the wind tunnel, it is not appropriate to simulate a wing at an angle of attack of 3° in the wind tunnel with the same angle of attack in free-air CFD computations. One modeling approach is to adjust the angle of attack to approximate the tunnel blockage effects and 3D-geometry effects. From the many RANS computations that Krimmelbein [20] ran at the reduced freestream Mach number of $M_\infty = 0.1$, Krimmelbein has derived a simple yet powerful algebraic relation that holds well across the configuration space relating the full 3D computation to a spanwise-infinite approximation, shown in Eq. (3):

$$\alpha_{ISW} \approx (0.0091\Lambda + 0.69)\alpha_{3D,WT} \tag{3}$$

*In the original report by Boltz et al. [14], not every geometric configuration has transition data at all 6 microphone locations. For example, at $\Lambda = 50°$ and $\alpha = -0.5°$, Boltz et al. only report transition data at $x_{tr}/c \in [0.21, 0.24, 0.30]$.

†Recall that the 4 in NACA $64_2$015A indicates the chordwise location of the pressure minimum in tenths of a chord for the zero-lift configuration, i.e., $\alpha = 0°$ for a symmetric airfoil [18, p. 5].

where α_{ISW} is the infinite-swept-wing angle of attack in the local frame as approximated by Krimmelbein [20]. Here, both Λ and $\alpha_{\mathrm{3D,WT}}$ are in degrees. Note that α_{ISW} indicates a rotation about the quarter-chord in the same way that α_{B} does. The values of α_{ISW}, however, are quite distinct from the geometrical α_B values: see Figure 1 for their distributions across $\alpha_{\mathrm{3D,WT}}$ and Λ for configurations with corresponding transition measurements by Boltz et al. [14]. For the same configuration, the geometric extremes of the test matrix show some differences of $|\alpha_{\mathrm{B}} - \alpha_{\mathrm{ISW}}| > 1^\circ$.

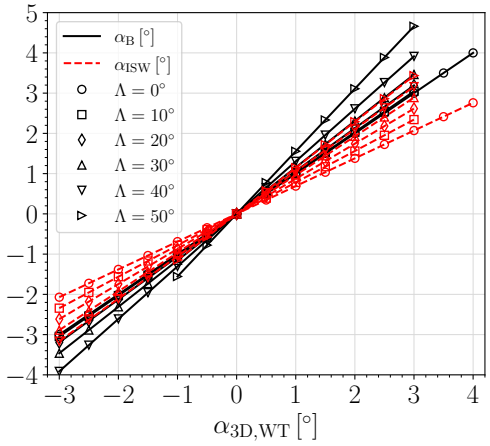

Fig. 1 The angle of attack in the local frame (solid black) compared with the infinite-swept-wing, blockage-correction approximation from Krimmelbein [20] (dashed red) against $\alpha_{\mathrm{3D,WT}}$. Distinct markers correspond to different sweep angles.

These values of α_{ISW} and β_{ss} are used to prescribe the freestream velocity vector orientation. We next discuss the details of the OVERFLOW solver, which was used to compute the partly laminar mean flow over the infinite-span swept wing.

C. OVERFLOW CFD Solver

The NASA OVERFLOW 2.4b code is an implicit, structured, overset-grid Navier-Stokes solver that can compute both time-accurate and steady-state solutions [21]. For this analysis, steady-state solutions are sought. The freestream Mach number is 0.27 and the freestream temperature is 303 K. The turbulence production is limited to downstream of the imposed transition location (detailed in Section II.A). All computations are performed by using the Spalart-Allmaras turbulence model with the rotation/curvature correction term enabled (SA-RC-neg-noft2, [22]). The freestream eddy viscosity is $\mu_{t,\infty}/\mu_\infty = 10^{-7}$ and the Roe upwind scheme is used along with an improved SSOR Jacobi algorithm for the linear solution. The local CFL number for each cell is based on the sum of the maximum eigenvalue in each coordinate direction, ramping between a lower bound of 1 and an upper bound of 1000. The turbulence-model time-step is 4 times the flow-solver time-step. Outflow boundary conditions are based on Riemann invariants with the freestream imposed on incoming characteristics. For $\Lambda \neq 0^\circ$, a 5-plane grid is generated in body-fitted coordinates, permitting a periodic boundary condition in the spanwise direction. The wing surface boundary condition is viscous no-slip and adiabatic, imposed by pressure extrapolation.

D. Grid Generation

All base flows considered in this work have been computed on a single grid, which has been generated using an automated procedure based on the maximum Reynolds number of $\mathrm{Re}_c = 40 \times 10^6$. A y^+ value of 0.25 at $x/c = 0.25$ based on an incompressible flat plate is used to approximate a constant Δy for the initial grid spacing off the surface over the entire wing [23]. The laminar boundary-layer thickness at quarter-chord is estimated as equal to $\delta = 5(c/4)/\sqrt{Re_{c/4}}$. A total of 326 nodes in the wall-normal direction are placed within the inner layer of the first 3δ, followed by a smooth expansion of 151 nodes in the outer layer out to $100c$. Each layer's cell growth is governed by hyperbolic-tangent stretching. Over the airfoil surface, a total of 721 streamwise points are used. Functions internal to Chimera Grid Tools (CGT) are used to control this distribution, namely, `hypgen`, `smogrd`, and `grided` [24]. For $\Lambda = 0^\circ$, a two-dimensional calculation is performed. For $\Lambda \neq 0^\circ$, the volumetric mesh contains 5 identical spanwise planes with a periodic flow

condition. In the freestream, the mesh cells asymptote to approximately isotropic cubes.

Checking grid quality when performing subsequent boundary-layer stability analysis is crucial, and for best practices, we check whether the wall-normal node spacing at the boundary-layer edge is $\Delta y < \delta/70$. Since this grid was generated based on flat-plate estimates at a high chordwise Reynolds number of 40 million, it is a natural question if this grid-quality metric is upheld at lower Reynolds numbers. Out of the cases run by Boltz et al. [14], the smallest Reynolds number is on the order of 4.6 million. Running OVERFLOW for this configuration at sweep 40° and angle of attack −3°, querying this metric on both sides of the wing near 5% x/c yields a spacing of about $\delta/72$. This confirms a reasonable grid quality for this case and is presumed to hold for the intermediate Reynolds numbers as well.

E. LASTRAC: Stability Analysis Tool

Version 3.1 of LASTRAC is a suite of codes for boundary-layer stability analysis across the speed regimes capable of Linear Stability Analysis (LST) and solving both Linear and Nonlinear Parabolized Stability Equations (LPSE/NPSE). In recent work, LASTRAC has been successfully coupled with the OVERFLOW [12, 17] and FUN3D flow solvers [16] for automatic transition prediction based on the N-factor method. The details on the stability methodology can be found in Chang [25] and will be summarized here. For stationary crossflow at nonzero sweep and Tollmien-Schlichting waves at zero sweep, the infinite-swept-wing assumption is used to model the growth of instabilities, using an orthogonal curvilinear coordinate system. For Tollmien-Schlichting waves at nonzero sweep, LASTRAC.3d is used, leveraging a nonorthogonal coordinate system. The growth of the disturbances is integrated from the first unstable location to compute the N-factor. For LST, the growth rate is given directly as the negative, imaginary component of the streamwise wavenumber $-\alpha_i$, whereas for PSE[‡], it is based on the integral of the disturbance kinetic energy profile at a given station. For stationary crossflow, the path of integration is perpendicular to the leading edge, while for TS, it is parallel to an inviscid streamline at the boundary-layer edge. This present approach of multiple trajectories in stability analysis is used to disambiguate the amplification of TS waves from that of traveling crossflow modes.

A fourth-order accurate finite difference is used in the interior of the grid in the wall-normal direction. For the boundaries, the order of accuracy is decreased to second-order. The wall-normal mapping used for all stability analysis is a dual-clustering, piecewise function. Clustering is applied near the wall and near the critical layer, and an equispaced grid is used in the inviscid region: see Eq. 45 from Ref. [25]. The clustering height y_c near the critical layer is defined as:

$$y_c = 0.85 \min\left(\delta_{99.5}, 2\delta_{50}\right). \tag{4}$$

Here, $\delta_{99.5}$ is the height in the boundary layer where the streamwise velocity profile $\overline{u}_s/\overline{u}_{s,e} = 0.995$, and similarly, δ_{50} is where $\overline{u}_s/\overline{u}_{s,e} = 0.50$. The streamwise velocity component $\overline{u}_s$ is aligned with the inviscid streamline angle $\psi_s \equiv \text{atan2}(\overline{w}_e, \overline{u}_e)$. These clustering functions have been implemented such that the user only needs to specify a nondimensional freestream node-spacing and the max height. In this work, $\Delta y_{\text{fs}}/\ell = 0.2$, and $y_{\max}/\ell = 60$, where ℓ is the local, similarity boundary-layer length scale defined by

$$\ell \equiv \sqrt{\frac{\overline{\nu}_e s}{\overline{u}_e}}, \tag{5}$$

where $\overline{\nu}_e$ is the kinematic viscosity at the end of the profile[§]. The streamwise grid used for stability computations is equispaced along the wing surface, discretized with first-order finite differences. For TS analysis at nonzero sweep angles, i.e., $\Lambda \geq 10°$, the step size was $\Delta s = 5\,\text{mm}$ ($\Delta s/c \approx 4.1 \times 10^{-3}$). However, for zero sweep, TS analysis without using the PNS approximation proved to be more sensitive to the PSE step-size criterion, demanding a larger step size of $\Delta s = 25\,\text{mm}$ ($\Delta s/c \approx 2.1 \times 10^{-2}$)[¶]. For SCF analysis, a higher resolution is required to appropriately resolve the growth rates near branch-I immediately downstream of the attachment line, so the step size $\Delta s = 0.75\,\text{mm}$ ($\Delta s/c \approx 6.2 \times 10^{-4}$) was selected.

[‡]In this manuscript, when the acronym "PSE" is used, the linear form of the methodology is implied.

[§]Note that the definition of ℓ in Eq. (5) reaches a supposed singularity at $s = 0$, the attachment line. However, $\overline{u}_e \to 0$ as $s \to 0$ as well, keeping ℓ finite. For all present computations, the streamwise distribution of ℓ near the attachment line does not experience any numerical divergence.

[¶]The TS PSE analysis over the specified frequencies still computes some divergent growth rates by violating the step-size criterion at $\Lambda = 0°$ and 50°. However, these frequencies do not define the envelope and are very low, nominally < 1000 Hz. They are filtered out in post-processing by considering the nonparallel growth rate and its streamwise derivative. On another note, given the significantly larger step size used for the $\Lambda = 0°$ configurations, it is natural to wonder if the PSE solutions are appropriately converged with the chosen streamwise resolution. The first-order solution is compared against the corresponding second-order solution for a representative case, demonstrating only $\Delta N = O(10^{-3})$, which is sufficiently small for this application. This low level of discrepancy allows us to label the TS PSE solutions converged in the s-direction.

For Tollmien-Schlichting (TS) analysis, the wave angle with respect to the streamline angle is set to zero. Frequencies are varied such that the envelope is well captured across the laminar extent of the wing for all considered configurations. For the relevant configurations, the dimensional frequency range is 1000 Hz − 21850 Hz, discretized with $\Delta f = 75$ Hz. When selecting the TS eigenmode from the spectrum, several eigenvalue filters are applied:

- The total disturbance wavelength is limited by $\lambda/\delta < 40$.
- The wall-normal derivative of the pressure eigenvector component at the wall is $\mathrm{d}\hat{p}/\mathrm{d}y|_{\mathrm{w}} > 10^{-12}$.
- The minimum allowable value of the nondimensional growth rate is $\alpha_i \ell = -0.2$.
- The 2D, nondimensional phase speed $c_{\mathrm{ph}} \equiv \omega/(\alpha_r \overline{u}_e)$ is positive and less than 1.

For stationary crossflow, the disturbances are computed following a 2D, leading-edge-orthogonal path down the wing. For internal verification of LASTRAC usage, it is prudent to check that SCF along the leading-edge-orthogonal path produces N-factors that are identical to SCF amplification computed along a 3D inviscid streamline. For instance, Chang [26] demonstrates this in Figure 4 from Ref. [26]. This internal verification has been performed for the present version of LASTRAC, and the plot will be omitted for brevity. Thus, even though the stationary crossflow amplification was determined using the chordwise trajectory normal to the leading edge, the results are equivalent to those obtained with the streamline trajectory used for the TS analysis. Spanwise wavelengths (in the direction parallel to the leading edge) are also varied such that the envelope is fully captured across the laminar extent of the wing for all considered configurations. The dimensional spanwise wavelengths λ_z range from 0.4 mm to 20 mm. For smaller sweep angles, higher Reynolds numbers are required to achieve transition onset under favorable pressure gradients, i.e., nominally $\alpha_{\mathrm{3D,WT}} \leq 1.5°$, so the high wavelengths up to 20 mm are often not relevant to the envelope computation. For these configurations, the wavelengths are clipped at 6 mm. Where permitting, this range is discretized as $\Delta\lambda_z = 0.1$ mm for sweep angles $\Lambda \in [40°, 50°]$. For lower sweeps, $\Delta\lambda_z = 0.05$ mm is required to adequately captured the envelope smoothly near the suction peak. When selecting the SCF eigenmode from the spectrum, several eigenvalue filters are applied (similar to TS):

- $\lambda/\delta < 40$.
- $\mathrm{d}\hat{p}/\mathrm{d}y|_{\mathrm{w}} > 10^{-12}$.
- The minimum allowable value of the nondimensional growth rate is $\alpha_i \ell = -0.025$.
- The disturbance wave angle $\psi_w \equiv \mathrm{atan2}(\beta, \alpha_r)$ with respect to the streamline angle $\psi_s \equiv \mathrm{atan2}(\overline{w}_e, \overline{u}_e)$ is restricted to $75° < \psi_w - \psi_s < 110°$.

For LST, the quasiparallel assumption is asserted and curvature of the wing is neglected in the stability equations. For PSE, the nonparallel eigenvalue problem is solved to initialize the disturbance. Let N_{ζ_1} be the number of points within the boundary layer for stability computations. First, the global eigenvalue problem is solved on a reduced boundary-layer, wall-normal resolution of $N_{\zeta_1} = 61$ points. Then the grid resolution is increased such that $N_{\zeta_1} = 121$ points are within the boundary-layer and the local eigenvalue problem is solved. Note for PSE, the PNS approximation is applied only to SCF analysis for the streamwise derivative of the pressure component of the shape-function $\partial\hat{p}/\partial s$. This allows finer streamwise steps by drastically reducing the step-size criterion—see Eq. 26 in Chang [25]. The present TS PSE stability analysis does not use the PNS approximation.

F. Sources of Error and Uncertainty

A primary source of modeling error is from assuming a spanwise-infinite flow when the experimental data are based off a finite-span wing in a test section of circular cross-section. There is additional modeling error incurred from using Krimmelbein's angle-of-attack relation in Eq. (3). Quoted from Boltz et al. [14], another source of measurement error is the following:

> A certain amount of scatter is present in the data, due to direction for finite angles of sweep. The lateral displacement of the detection stations (in the direction normal to the free stream) increased with sweep angle, thereby increasing the possibility of having three-dimensional flow effects appear in the data [14].

Additionally, there were leaks that primarily affected the measured transition location of sweep angles $\Lambda = 0°$ and $10°$. Specifically:

> Because of several small leaks, which developed in the internal tubing to the orifices on the upper surface, where the microphones were connected, the pressure distributions presented in the report are those which were measured on the lower surface. These leaks did not have any significant effect on the transition data obtained for sweep angles greater than 10°.

Another source of error in the measured data is related to ascertaining the transition location, adding some uncertainty to each transition-location measurement for sweep angles $\Lambda \geq 20°$. Boltz et al. [14] state:

> The data for sweep angles of 20°, 30°, 40°, and 50° were obtained by increasing the tunnel speed until the onset of transition occurred at successive detection (orifice) stations, beginning at the rear and moving forward. At sweep angles of 0° and 10°, however, it was necessary to isolate individual orifices from contamination, when making transition measurements, by plugging the orifices ahead of the one being considered.

In other words, for sweep angles $\Lambda \geq 20°$, if the experiments report a measured transition location of $x_{\text{tr}}/c = 0.30$, this is based on recognizing the onset of transition at the next-upstream microphone at $x/c = 0.24$. This methodology inherently carries a specific uncertainty to each transition measurement based on position, which has been presently neglected in computations. On another note, Boltz et al. [14] report that the flow in the test section has a maximum helix angle of 0.25°, which is not modeled in the present simulations. Lastly, the freestream temperature is not reported by Boltz et al. [14]. A value of $T_\infty = 303$ K is assumed for the present computations to agree with Krimmelbein [20].

III. Results

A. OVERFLOW Convergence

The mean-flow residual histories of three selected OVERFLOW solutions are given in Figure 2. The first solution corresponds to a representative unswept case with the following configuration: $(\Lambda, \alpha_{3\text{D,WT}}, x_{\text{tr}}/c) = (0°, 4°, 0.21)$ with a Reynolds number 6.27×10^6. The second solution is a moderately swept configuration with $(30°, -3°, 0.21)$ and $\text{Re}_c = 7.13 \times 10^6$, whereas the third solution is a strongly swept configuration with $(50°, -1°, 0.24)$ and $\text{Re}_c = 7.36 \times 10^6$. The horizontal axis shows the OVERFLOW flow-solver iterations. The vertical axis shows the base-10 logarithm of the L^2-norm of the mean-flow residual starting with an initial value of zero[‖]. All cases achieve nearly 14 relative orders of magnitude of convergence, although as sweep increases, the number of iterations to reach the numerical floor increases. This trend is common across all configurations computed[**].

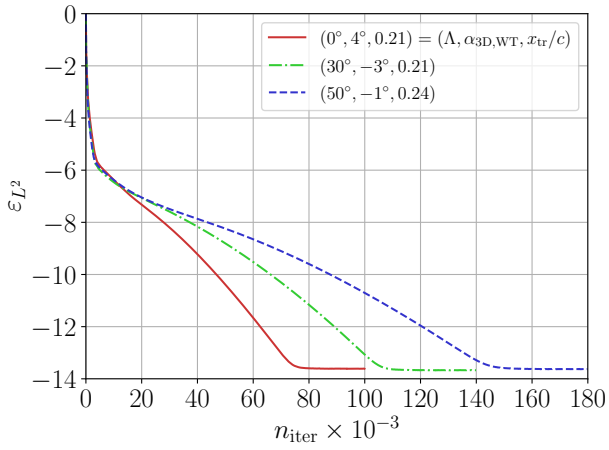

Fig. 2 Relative residual convergence histories for three representative configurations.

B. Pressure Coefficients: Validation

The base flows are presented in terms of the chordwise distribution of surface pressure coefficients for the upper surface, which allows the computed basic-state characteristics to be compared with the experimental measurements

[‖] By L^2-norm of the mean-flow residual, we mean the L^2-norm of the five evaluated equations of conservation of mass, momentum, and energy, each weighted by cell volume raised to the 2/3 power.

[**] Another trend not pictured is that as the freestream Reynolds number increases (with all else constant), the number of iterations decreases to converge the residual to the numerical floor.

by Boltz et al. [14]. Experimental pressure measurements were taken at atmospheric pressure conditions, i.e., $\mathrm{Re}_c = 7.29 \times 10^6$. To validate against experimental transition measurements, the simulations were initialized as laminar and transitioned to turbulent artificially downstream near $x_{\mathrm{tr}}/c = 0.45$. The partly laminar solution whose Reynolds number is closest to 7.29×10^6 is selected for each geometric configuration. Figure 3 shows the C_p vs. x/c for selected configurations as computed by OVERFLOW, as well as the measurements by Boltz et al. [14]. Recall that Boltz et al. performed these measurements at two spanwise stations, which are referred to as the inboard and outboard stations, respectively. An important take-away from this figure is the accuracy of surface pressure predictions based on Krimmelbein's angle-of-attack relation of Eq. (3). As an example, OVERFLOW predictions for a spanwise-infinite swept wing ($\Lambda = 50°$) in free flight at $\alpha_{\mathrm{ISW}} = 1.145°$ are seen to match well with the measured, inboard C_p at $\alpha_{\mathrm{3D,WT}} = 1.0°$. Additionally, note that the inboard measurements tend to agree more closely with the OVERFLOW simulations rather than the outboard measurements. For configurations that lead to an extended region of favorable pressure gradient (e.g., $\alpha_{\mathrm{3D,WT}} = -3.0°$), the spanwise pressure gradients in the experimental measurements are observed to be small, i.e., the inboard and outboard stations measure similar surface pressures. In the presence of an adverse streamwise pressure gradient from $x/c \approx 5\%$–20%, however, there are greater three-dimensional effects and the spanwise pressure gradient is appreciable, e.g., see the measurements at $\alpha_{\mathrm{3D,WT}} = 3.0°$. Downstream of $x/c \approx 0.50$, the OVERFLOW solutions start to diverge from the measured C_p. This is acceptable, as that interval on the model is likely turbulent and, hence, irrelevant for laminar stability analysis.

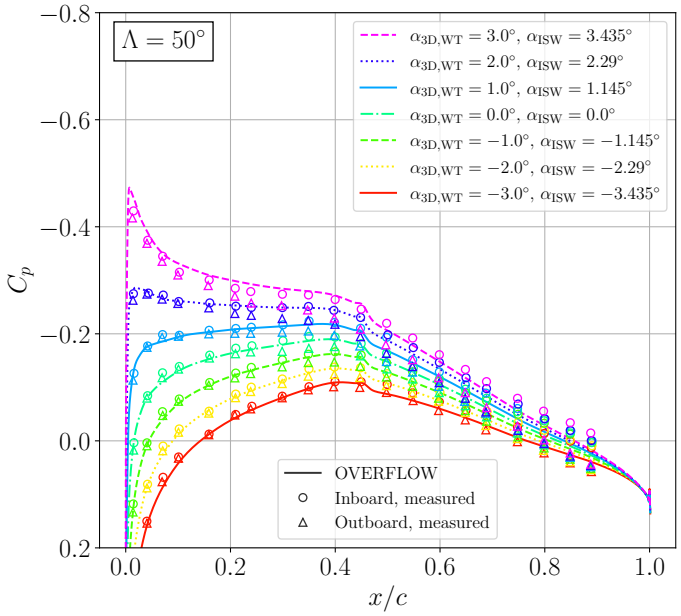

Fig. 3 Chordwise surface pressure coefficient vs. x/c. OVERFLOW results are compared to inboard and outboard measurements by Boltz et al. [14]. Angles of attack vary from $\alpha_{\mathrm{3D,WT}} = -3°$ to $3°$. The sweep angle is $50°$. OVERFLOW solutions are artificially tripped to turbulence near $x/c = 0.45$.

Let us consider the C_p comparison at sweep $30°$, as shown in Figure 4. There is strong agreement between simulation and experiment, however, the match is slightly worse than that of $\Lambda = 50°$ in the previous Figure 3, suggesting that the accuracy of Krimmelbein's relation in Eq. (3) between $\alpha_{\mathrm{3D,WT}}$ and α_{ISW} may have reduced slightly in this case.

Finally, let us consider the two-dimensional limit ($\Lambda = 0°$) for this validation. Even though this model is at $\Lambda = 0°$, recall that the model is semispan and has a rounded tip Boltz et al. [14, Figure 1], producing finite-wing effects and discrepancies between the measurements at the outboard and inboard stations. In Figure 5, the pressure coefficients between OVERFLOW and experimental measurements somewhat deviate from one another. For these configurations, the accuracy of Krimmelbein's relation in Eq. (3) between $\alpha_{\mathrm{3D,WT}}$ and α_{ISW} has slightly reduced: see, also, Figure 47 in Krimmelbein [20] for a demonstration of this deviation at $\alpha_{\mathrm{3D,WT}} = 1.5°$ and $3°$. With that being said, it is important to note that the measured pressures for this configuration are appreciably spanwise-varying, especially for the angles of attack with adverse pressure gradients from $x/c = 5\%$–20%. As a result, any spanwise-infinite approach is bound to incur appreciable CFD error for this data.

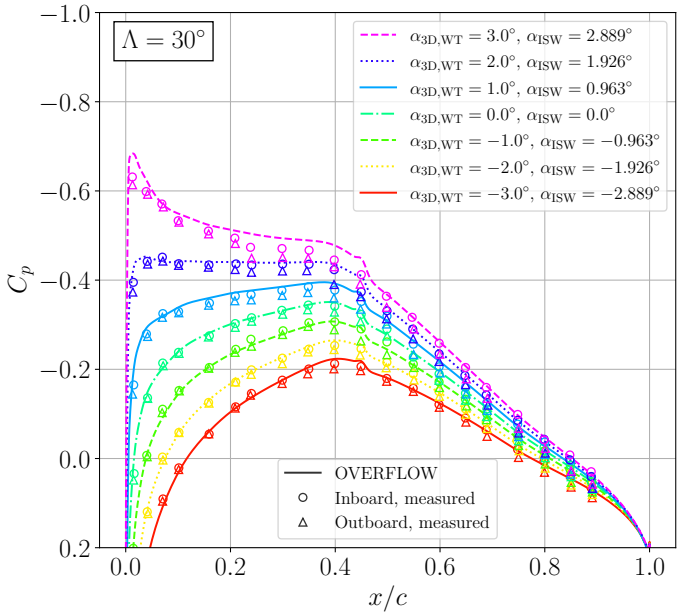

Fig. 4 Continuation of Figure 3 at $\Lambda = 30°$.

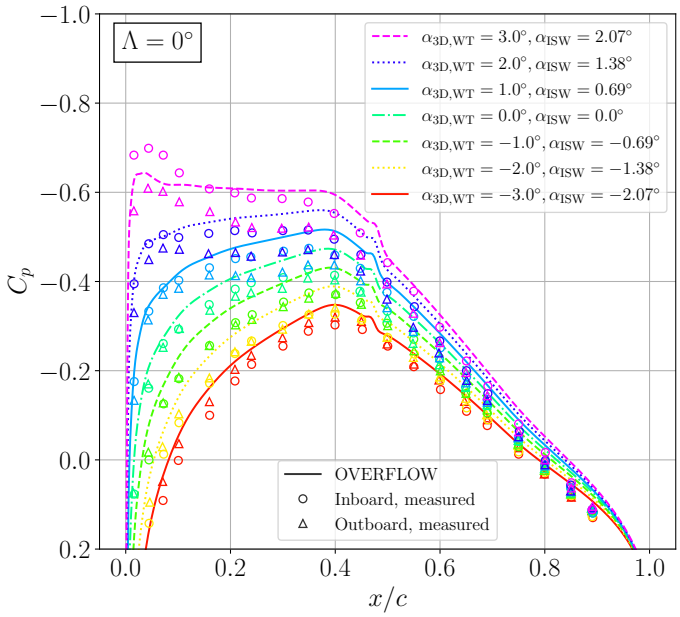

Fig. 5 Continuation of Figure 3 at $\Lambda = 0°$.

C. Stability Analysis: Verification

There are several other cases in the literature where stability analysis has been performed on the vast array of experimental measurements by Boltz et al. [14]. One of those is Zhu et al. [27], who performed TS analysis and demonstrated LST N-factors for the configuration $(\Lambda, \alpha_{3D,WT}, x_{tr}/c) = (10°, 0°, 0.45)$ at $\mathrm{Re}_c = 15 \times 10^6$. Figure 6 shows the digitized envelope of TS N-factors based on the LST computations by Zhu et al., plotted against x/c and those results are against present computations of N-factor curves for several frequencies. It is clear that there is strong agreement between the two simulations—the present computations reach $N_{TS,crit} \approx 10.7$ whereas Zhu et al. predicted $N_{TS,crit} \approx 11.1$. A difference of $\Delta N = 0.4 < 1$ is considered acceptable for this verification, especially given the high

local growth rates of TS instabilities near $x_{tr}/c = 0.45$.

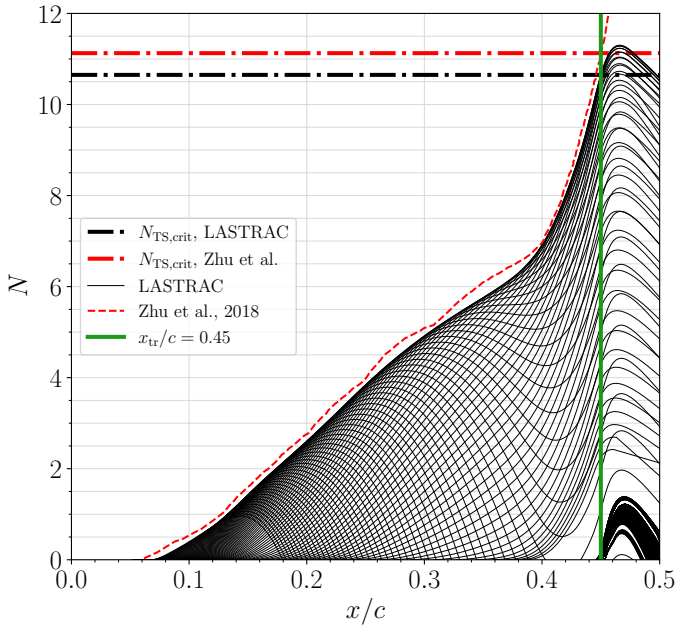

Fig. 6 Tollmien-Schlichting verification against Zhu et al. [27]. LASTRAC LST N-factors are shown in black and Zhu et al.'s LST TS envelope is shown in dashed red. The green vertical line indicates the measured transition location from Boltz et al. [14], whereas the dash-dotted lines indicate the respective values of the envelope N-factor at the measured transition location.

We also compare our predictions of stationary crossflow amplification with the LST N-factors of Zhu et al. [27] for $(\Lambda, \alpha_{3D,WT}, x_{tr}/c) = (40°, -1.5°, 0.35)$ at $\mathrm{Re}_c = 6.30 \times 10^6$. Figure 7 shows the digitized version of Zhu et al.'s envelope of SCF N-factors against x/c, compared against the present computations based on LST. Similarly, it is clear that there is strong agreement between the two curves—the present computations reach an $N_{SCF,crit} \approx 7.8$ whereas Zhu et al.'s $N_{SCF,crit} \approx 7.5$. A difference of $\Delta N = 0.3 < 1$ is considered acceptable for this verification.

Another relevant case from the literature is that of Diakakis et al. [28], who demonstrate the trend of the N-factor contours versus Reynolds number. However, Diakakis et al. do not use the same methodology as the present computations: they use an Orr-Sommerfeld database from XFOIL to output the growth rate $\alpha_i = \alpha_i(H, \mathrm{Re}_\theta, f)$, i.e., as a function of the boundary-layer shape-factor, momentum-thickness Reynolds number, and disturbance frequency, respectively. The growth rate is then integrated in space to determine the N-factor. Therefore, a quantitative numerical comparison is not appropriate given the distinct methodologies, but instead, a qualitative comparison matching the trend in Reynolds number is appropriate. Diakakis et al. considered the sweep angle 0° and the angles of attack of 0° and 1°. Figure 8 shows the transition location versus Reynolds number for selected values of the transition N-factor for both angles of attack. LASTRAC N-contours based on LST are plotted for $N \in [8.0, 9.5]$, $\Delta N = 0.5$, and N-contours of Diakakis et al. are plotted for $N \in [9.5, 11.5]$, $\Delta N = 1.0$. For $\alpha_{3D,WT} = 0°$, the LASTRAC predictions indicate a decrease in transition N-factor of about 1.5 across the range of Reynolds numbers from the experiment. The results of Diakakis et al. only experience a $\Delta N_{TS} \approx -1.0$. Given the distinct methodologies, a discrepancy of this type is considered acceptable. For $\alpha_{3D,WT} = 1°$, both LASTRAC computations and the Diakakis et al. results undergo a $\Delta N_{TS} \approx -1.5$. Despite the differences in the absolute values of N_{TS}, the comparable variations in N_{TS} as a function of the Reynolds number demonstrate a successful cross-comparison between both methodologies.

With these cases serving as external verification, let us now move forward to stability analysis, comparing the predictions of LST and PSE for TS and SCF N-factors.

D. TS N-factors at Unswept Conditions

The stability analysis of other researchers for the wide array of experimental measurements has only been performed using Linear Stability Theory (LST) [20]. However, one should bear in mind that, while LST remains a powerful linear

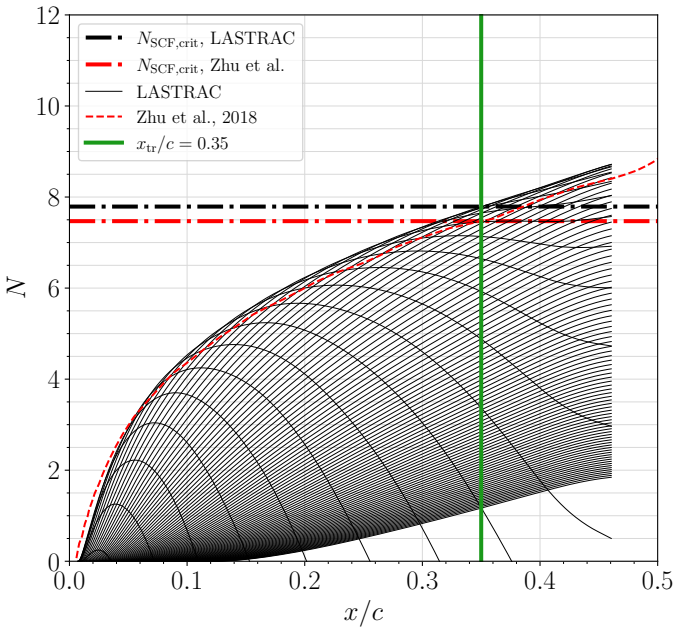

Fig. 7 Stationary crossflow verification against Zhu et al. [27]. LASTRAC LST N-factors are shown in black and Zhu et al.'s LST SCF envelope is shown in dashed red. The green vertical line indicates the measured transition location from Boltz et al. [14], whereas the dash-dotted lines indicate the envelope's respective values at the transition location.

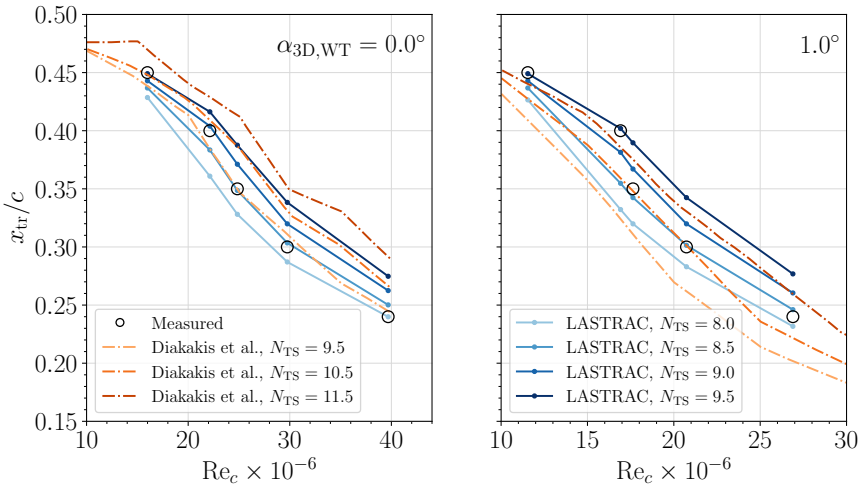

Fig. 8 Tollmien-Schlichting N-factor contours for verification with Diakakis et al. [28] at $\Lambda = 0°$ and at two angles of attack: $0°$ (left) and $1°$ (right). Measurements by Boltz et al. [14] are shown in open circles. LASTRAC N-factor contours are shown in blue–darker blue indicating a higher value. Diakakis et al. N-factor contours are similarly shown in orange.

stability method, unlike PSE, it does not account for nonparallel mean-flow effects and for the effect of streamwise curvature on disturbance growth. We now consider the critical N-factor variation versus Re_c at $\Lambda = 0°$ for the various angles of attack. The LST results are shown on Figure 9(a), whereas the right Figure 9(b) shows the PSE results. Each point in the figure corresponds to a distinct configuration as tested by Boltz et al. [14]. The colors correspond to different transition locations, i.e., to different values of Re_c, while $\alpha_{\mathrm{3D,WT}}$ in degrees is displayed directly in the scatter plot as markers. The zeroth-order least-squares fit is shown as a horizontal line through the data, while the

first-order fit is shown with a negative slope. The zeroth-order fits show transition N-factors of $N_{\mathrm{TS,crit}} = 8.7$ for LST and 8.9 for PSE. This demonstrates that the combined effect of mean-flow nonparallelism and surface curvature is minor but destabilizing. This effect is also observed in the vertical-axis intercepts of the first-order fits, given by $N_{\mathrm{TS,crit}} = -0.030(\mathrm{Re}_c \times 10^{-6}) + 9.3$ for LST and $N_{\mathrm{TS,crit}} = -0.037(\mathrm{Re}_c \times 10^{-6}) + 9.6$ for PSE. These results serve as the basis of model calibration for TS-dominated transition at $\Lambda = 0°$.

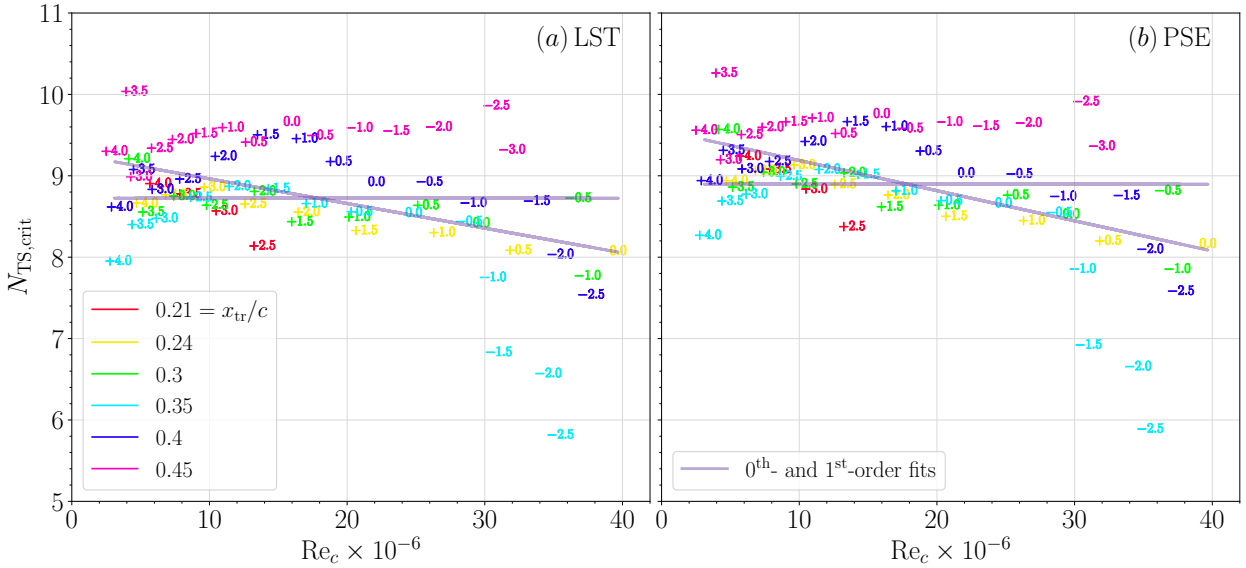

Fig. 9 Critical N-factor for TS as a function of chord Reynolds number for $\Lambda = 0°$. Markers directly indicate $\alpha_{\mathrm{3D,WT}}$ in degrees, while the marker colors indicate the measured transition location. Zeroth- and first-order fits are shown in purple lines: (a) LST results, and (b) PSE results.

E. TS/SCF Dual N-factors at Swept Conditions

Predicting the onset of transition at nonzero sweep requires one to account for the potential role of stationary crossflow (SCF) disturbances. The effects of mean-flow nonparallelism and surface curvature are essential to properly characterize the SCF development. In general, nonparallel effects tend to increase the amplification of stationary crossflow disturbances, while streamwise-curvature effects appreciably stabilize the disturbance [29, Fig. 13]. Figures 10, 11, 12, and 13 show the dual N-factor scatter plots for sweep angles [20°, 30°, 40°, 50°], respectively. These plots demonstrate the amplification of TS against SCF amplification at the measured transition location along the wing. The left subplots (i) show the LST results while the right subplots (b) show the PSE results.

From these figures, a representative $N_{\mathrm{SCF,crit}}$ can be calibrated for the SCF-dominant cases with negligible TS amplification. These configurations lie on the N_{SCF}-axis or very close to it, and correspond to highly favorable pressure gradients which drastically stabilize the Tollmien-Schlichting waves. Across the sweep angles $\Lambda \geq 20°$, for LST, the critical N-factor for SCF disturbances is roughly $N_{\mathrm{SCF,crit}} \approx 7.5$, whereas for PSE, there is slightly greater amplification: $N_{\mathrm{SCF,crit}} \approx 8$.

The shape of the transition locus away from the horizontal and vertical axes of the dual N-factor plots provides some insights into the degree of interaction between the TS and crossflow instability mechanisms. For instance, a nearly rectangular locus is indicative of nearly zero interaction between the two mechanisms, i.e., transition onset if either due to TS alone or due to crossflow. As the data becomes more elliptical (convex), diagonal, or even 'subdiagonal' (concave), it reflects a greater degree of interaction between TS and SCF.

Let us first consider the LST results in isolation as the sweep angle is increased. At lower angles, such as $\Lambda = 20°$, the data indicate a low level of TS/SCF interaction from this linear analysis, since the locus shape is approximately rectangular (see Figure 10). As sweep is increased, the locus of data becomes more elliptical (see Figures 11 and 12). Finally, at $\Lambda = 50°$, the LST data in Figure 13 are diagonal. From the LST data, it would then appear that as the sweep is increased, the TS/SCF interaction grows stronger.

Now consider the PSE results. At the sweep angle of 20°, the locus of data is primarily diagonal (see Figure 10),

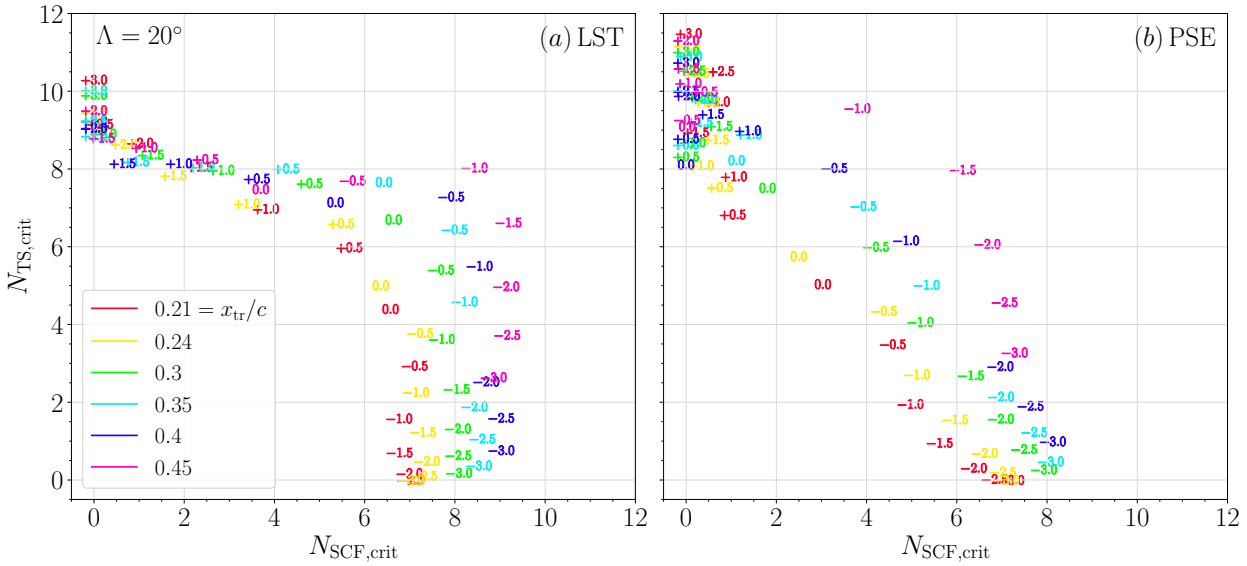

Fig. 10 Dual N-factors at measured transition locations for $\Lambda = 20°$. Markers directly indicate $\alpha_{3D,WT}$ in degrees, while the marker colors indicate the measured transition location: (a) LST results, and (b) PSE results.

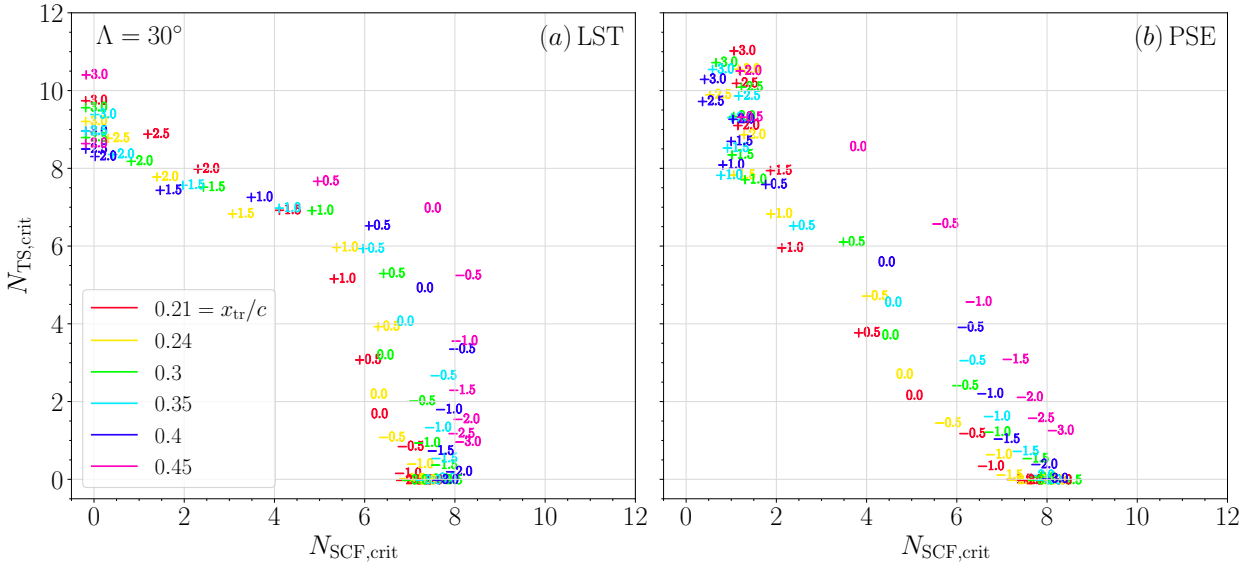

Fig. 11 Continuation of Figure 10 at $\Lambda = 30°$.

with the exception of the transition front for $x_{tr}/c = 0.45$ that appears to be more elliptical. As sweep increases, the locus of the PSE data no longer intercepts the N_{TS}-axis, i.e., the SCF amplification is now nonzero at the transition location, as crossflow becomes more destabilized with increasing sweep (see Figure 11 and 12). Despite that change, the trend remains aligned with the diagonal across all of the configurations. At the highest sweep angle of 50°, the interaction between TS and SCF becomes even stronger and is seen as 'subdiagonal', or concave (see Figure 13).

Comparing LST to PSE laterally across these figures, there are multiple trends visible at once. Near the N_{TS}-axis, the results show that there are low levels of SCF amplification now captured in PSE that LST did not compute, and TS is slightly more destabilized. This graphically shifts the data up and slightly to the right on the N_{TS}-axis. On the N_{SCF}-axis, PSE shows slightly higher SCF growth than LST does for the corresponding configurations with highly favorable pressure gradients, shifting the data to the right. However, moving away from the N_{SCF}-axis and considering the mixed-mode configurations, TS becomes more destabilized in PSE than in LST, and SCF becomes *stabilized* in PSE

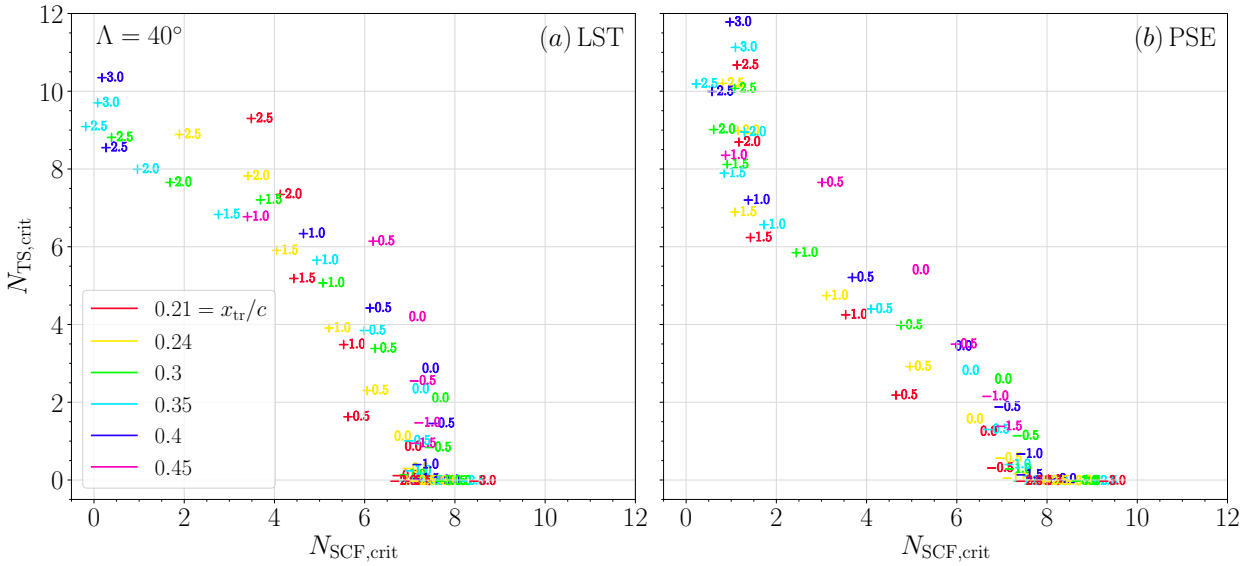

Fig. 12 Continuation of Figure 10 at $\Lambda = 40°$.

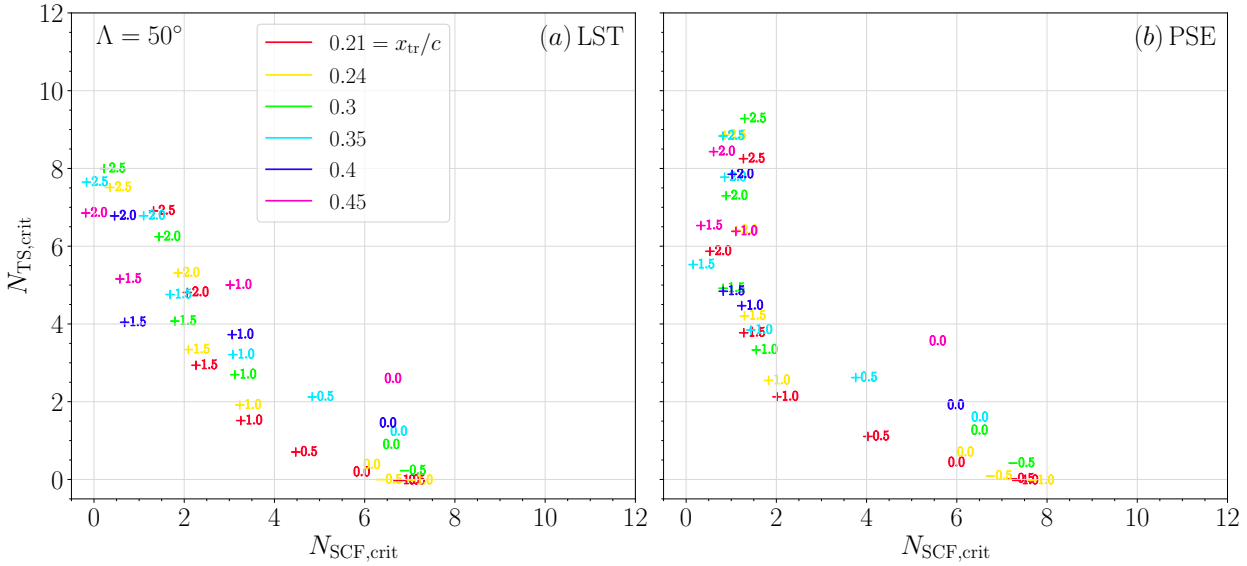

Fig. 13 Continuation of Figure 10 at $\Lambda = 50°$.

with respect to the results of LST. Graphically, this shifts the results up and to the left. Overall, the trends for PSE seem to predict a higher level of interaction between TS and SCF, as the loci of data are more diagonal for $\Lambda \leq 40°$ and even concave for $\Lambda = 50°$.

When considering these various linear metrics to anticipate the TS/SCF interaction, there are alternate approaches that consider the physical problem differently. For example, considering the critical N-factor only at the measured transition location x_{tr}/c has the side-effect that local maxima in SCF N-factor distributions upstream of x_{tr}/c are ignored entirely. As an example, consider in Figure 14 the PSE SCF distribution of N-factors corresponding to a case with both appreciable SCF and TS amplification: $(\Lambda, \alpha_{3D,WT}, x_{tr}/c) = (20°, 0°, 0.3)$. The critical N-factor for this case is only 1.8, whereas the maximum value of the envelope upstream of the measured transition location x_{tr}/c is 3.2. This upstream SCF amplification may be relevant for some pathways to transition, as the upstream crossflow vortex modulates the mean-flow appreciably and potentially establishes the conditions for significant resonant growth through secondary mechanisms—see Herbert [30] for details. In this spirit then, another approach for visualizing this wide array

of data is through the nonlocal metric where the maximum of the SCF N-factor envelope (which may occur upstream of x_{tr}/c) is selected rather than the critical SCF N-factor. Consider this nonlocal metric applied to $\Lambda = 20°$ for PSE in Figure 15. Comparing this to Figure 10(b), now the configurations near the N_{TS}-axis are off-axis, appropriately showing the nonzero SCF amplification experienced over the wing. Overall, for configurations with mild SCF growth, this metric has the effect of graphically shifting the loci of data to the right with respect to the $N_{SCF,crit}$-metric. For configurations with appreciable SCF amplification, the maximum of the N_{SCF} envelope moves to $x = x_{tr}/c$, so the value of the $\max_{x \le x_{tr}} N_{SCF}$-metric is identical to that of the $N_{SCF,crit}$-metric.

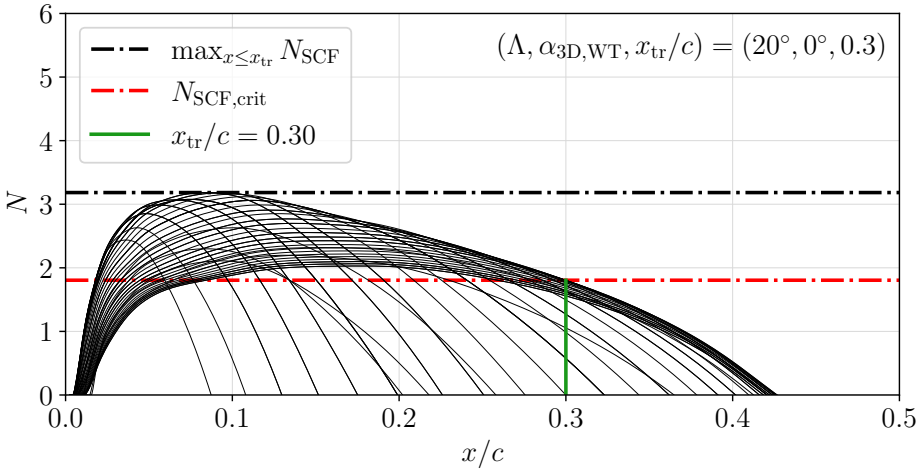

Fig. 14 Stationary crossflow PSE N-factors for several wavelengths are shown in black for a mixed-mode configuration. The black horizontal line indicates the overall maximum of the N-factor envelope upstream of the measured transition location, the red horizontal line indicates the critical N-factor, and the green vertical line indicates the measured transition location from Boltz et al. [14].

F. Discussion

The results presented in the previous Section III.E are based on several assumptions in the spirit of reduced-order methods, but have yet to be rigorously verified against higher fidelity methods. Because of this, the conclusions from this data should be seen as preliminary—a progress report of ongoing work.

Previous work by Krimmelbein [20] used LST to define the map of N-factors at the measured transition locations in the N_{TS}-N_{SCF} plane and found a relatively tight, rectangular distribution [20, Fig. 53(b)], indicating minimal interaction between the two modes of transition. The calibrated LST critical N-factors selected were $N_{TS,crit} = 12$ and $N_{SCF,crit} = 7.5$. On the other hand, the LST results in Section III.E showed that the locus of data in the N_{TS}-N_{SCF} plane varied from rectangular, to elliptical, to diagonal (depending on the sweep angle), indicating a stronger interaction between the TS and CF modes of transition. The main differences between the methodologies employed in the two works are outlined below in decreasing order of the anticipated degree of discrepancy:

1) Figure 53(b) of Krimmelbein [20] is based on full, 3D simulations of the model in the wind tunnel, whereas the present computations leverage only the spanwise-infinite assumption. From the measurements shown in Figure 5, it is clear that spanwise effects are more noticeable for configurations with adverse pressure gradients from 5%–20%, e.g., $\alpha_{3D,WT} \ge 2.5°$ at $\Lambda = 0°$, so the discrepancy between the present results and those of Krimmelbein [20] is anticipated to be greater for these configurations. Additionally, the error incurred from the angle-of-attack relation of Eq. (3) is slightly larger for smaller sweep angles. This causes the present stability computations to use pressure distributions that deviate further from both the full, 3D simulations of Krimmelbein and the experimental measurements. These observations likely contribute to the fact that Krimmelbein selected a nominal $N_{TS,crit} = 12$ across all sweep angles compared to the present result of $N_{TS,crit} = 8.7$ at $\Lambda = 0°$.
2) Krimmelbein [20] performed a scaling argument based on incompressible boundary-layer theory: "boundary-layer profiles are computed for a certain Reynolds number with a RANS solver and then scaled to emulate the behaviour of the same boundary layer at a different Reynolds number (Krimmelbein [20], p. 128). This

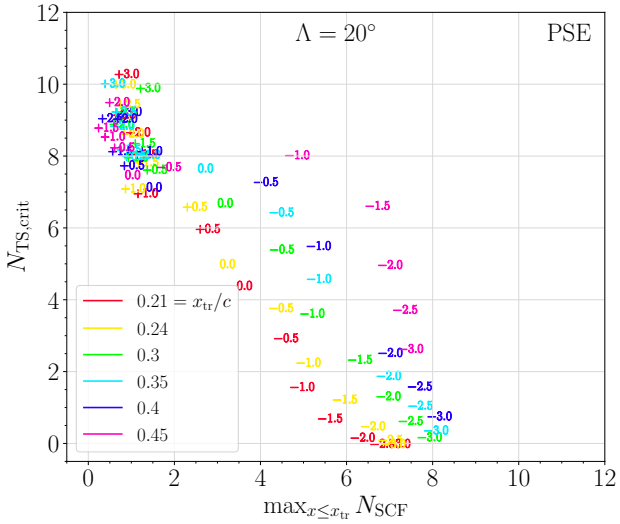

Fig. 15 Critical TS N-factor versus max SCF N-factor upstream of x_{tr}/c for the considered configurations at $\Lambda = 20°$. Markers directly indicate the angle of attack $\alpha_{\mathrm{3D,WT}}$ in degrees, while the marker colors indicate the measured transition location. Compare this with the dual N-factor chart in Figure 10(b).

methodology is a reduced-order approach, permitting Krimmelbein to perform only 42 basic-state computations for the entire configuration space, and run stability analysis on distinct configurations by this scaling argument. It is a novel approach used to simplify the wide array of experimental data. However, the present computations do not include this simplification and instead computes the basic state for each distinct configuration.

3) Krimmelbein computed all basic states at a Mach number of 0.1, which includes the cases that generated the angle-of-attack relation of Eq. (3) [20, p. 55]. The present computations used $\mathrm{M}_\infty = 0.27$ to retain as much physical relevancy to the experimental conditions as possible, yet still used the angle-of-attack relation derived by Krimmelbein.

These results serve as a useful step in the direction of transition modeling applied to a large database of measurements involving both TS- and crossflow-related transition scenarios.

IV. Summary and Concluding Remarks

The primary objective of this paper is to calibrate the linear boundary-layer stability characteristics for the NACA 64_2015A transition experiments in the NASA Ames 12-Foot Low-Turbulence Pressure Tunnel [14]. The objective is met by quantifying the evolution of linear disturbances present in the boundary layer by integrating the growth rates of both Linear Stability Theory (LST) and the Parabolized Stability Equations (PSE).

The basic states of the various experimental configurations are obtained with a spanwise-infinite assumption with OVERFLOW 2.4b. The computational grid has been generated using standard methods within Chimera Grid Tools. The infinite-swept simplification employed in this study neglects the three-dimensional effects associated with the finite span wing installed in the tunnel. However, it enables a computationally efficient way of exploring the wide array of nearly 365 configurations of sweep angles, angles of attack, and Reynolds numbers. The selected configurations correspond to the 6 sweep angles of $[0°, 10°, 20°, 30°, 40°, 50°]$, and the 13 angles of attack of $[-3°, 3°]$ with an increment of $0.5°$ with two additional angles of attack equal to $3.5°$ and $4°$ for $\Lambda = 0°$. Reynolds numbers are varied in the wind tunnel for each geometric configuration until transition is indicated at the locations of the microphones submerged below the model surface. These microphones are located at $x_{\mathrm{tr}}/c \in (0.21, 0.24, 0.30, 0.35, 0.40, 0.45)$ along the model. The spanwise-infinite approach is made possible by using the angle-of-attack relation developed by Krimmelbein [20] that allows an adjustment of the angle of attack. Blockage and three-dimensional effects are approximated by adjusting the input angle of attack to the spanwise-infinite simulation based on the relation derived by computing the full, 3D simulations of the model in the wind tunnel.

Stability analysis has been performed using version 3.1 of LASTRAC, scanning a large range of Tollmien-Schlichting (TS) frequencies and stationary crossflow (SCF) spanwise wavelengths. For 2D cases, TS evolution follows a path

orthogonal to the leading edge. For 3D cases, TS evolution follows an inviscid streamline at the boundary-layer edge as an integration path, whereas SCF evolution follows a leading-edge-orthogonal path.

For basic-state computations using the OVERFLOW solver, the L^2-norm of the residuals is shown to achieve nearly 14 orders-of-magnitude reduction until reaching the numerical floor. Pressure coefficients for sweep angles $[0°, 30°, 50°]$ are successfully validated against experimental measurements.

Tollmien-Schlichting evolution using LST has been verified for a representative case at $\Lambda = 10°$, $\alpha_{3D,WT} = 0°$, and $\mathrm{Re}_c = 15 \times 10^6$ against computations by Zhu et al. [27]. The two predictions agree well, with the difference in critical N-factors being less than 0.4, with $N_{TS,crit} = 7.8$ in our computations. Similarly, stationary crossflow evolution using LST has been verified against the published results [27] for a representative case with $\Lambda = 40°$, $\alpha_{3D,WT} = -1.5°$, and $\mathrm{Re}_c = 6.30 \times 10^6$. Again, the results agreed well, with a minor discrepancy of $N_{SCF,crit} < 0.3$. Additional comparisons are shown for TS computations at $\Lambda = 0°$ for $\alpha_{3D,WT} = 0°$ and $1°$ with respect to the data from Diakakis et al. [28].

Tollmien-Schlichting computations at sweep angle $\Lambda = 0°$ are summarized through their critical value $N_{TS,crit}$ at the transition location x_{tr}/c versus Reynolds number variation. Least-square fits demonstrate a zeroth-order value for $N_{TS,crit} = 8.7$ for LST and $N_{TS,crit} = 8.9$ for PSE, which serve as model calibration for TS-dominated flows.

Swept configurations at $\Lambda \in (20°, 30°, 40°, 50°)$ undergo significant amplification for both Tollmien-Schlichting and stationary crossflow. Dual N-factor charts are shown, plotting $N_{TS,crit}$ against $N_{SCF,crit}$ at the measured transition location. Stationary crossflow critical N-factors are calibrated to $N_{SCF,crit} = 7.5$ for LST and $N_{SCF,crit} = 8$ for PSE for SCF-dominant configurations.

Trends of the dual N-factor loci are discussed. In the N_{TS}-N_{SCF} plane, PSE predicts a more diagonal shape to the locus of data rather than a rectangular one. This is referred to as a higher level of TS/SCF interaction, since a rectangular shape would indicate little to no interaction between TS and SCF. For these computations, PSE SCF results are stabilized at the transition location with respect to the corresponding LST computation. For LST, the transition locus in the N_{TS}-N_{SCF} plane is nearly rectangular at sweep 20°, becomes more elliptical as sweep is increased to 30° and 40°, and reaches a diagonal trend at 50°. For PSE, a diagonal trend is observed for 20°, 30°, and 40°, and becomes 'subdiagonal' or concave at 50°. Overall, these findings point to a higher interaction between the TS and crossflow mechanisms with increasing sweep, regardless whether LST or PSE are used to predict transition.

An alternate visualization to the dual N-factor envelope corresponds to the maximum N-factor of stationary crossflow upstream of the transition location. This metric allows the effect of peak SCF amplification near the leading edge to be included in the dual N-factor criterion. However, further work is required to determine if it represents an improvement, especially in a broad number of cases. Using this metric, configurations with mild SCF amplification are more physically accurately represented in the dual N-factor chart, including the peak upstream SCF amplification.

Comparisons with the computational predictions by Krimmelbein [20] are discussed, highlighting the differences in the respective methodologies and potential sources of discrepancy in the dual N-factor charts. The potential sources include: a) the results from Ref. [20] were based on fully 3D basic state computations of the finite-span, installed wing. performed full, 3D simulations compared to the present spanwise-infinite simulations, b) Krimmelbein used a scaling argument to reduce the number of basic states computed, and c) a Mach number of 0.1 in Ref. [20] as against the present computations at $\mathrm{M}_\infty = 0.27$ to retain physical relevancy to the experimental conditions.

Future work will use these calibrated models on TS and SCF to predict transition and quantify the modeling error. The best-fit boundary between the laminar and turbulent regions in the N_{TS}-N_{SCF} plane may be formed as an ellipse, as in

$$\left(\frac{N_{TS}}{N_{TS,crit}}\right)^{a_{TS}} + \left(\frac{N_{SCF}}{N_{SCF,crit}}\right)^{a_{SCF}} = 1. \tag{6}$$

The LHS of Eq. (6) will be referred to as the indicator function based on the dual N-factor criterion. The parameters of the indicator function will be calibrated based on a subset of the data, while the remaining data will be used to validate the calibrated curve. The error will be assessed between the experimentally measured and calibrated data across the complete parameter space. The sensitivity of the model parameters to the selected subset of test conditions will be evaluated by using multiple subsets of the measurement data for the calibration process. Different transition criteria will be considered and their effect on transition prediction will be quantified to measure the sensitivity of the problem. For example, the transition prediction using a constant $N_{TS,crit}$ and $N_{SCF,crit}$ will be compared against that of an elliptical indicator function of Eq. (6). The role of traveling crossflow modes will be examined. Lastly, full 3D simulations of the model wing in the test section will be performed.

Appendix

A. Supplementary Visualization of TS/SCF Dual N-factors

For completeness, the application of the nonlocal metric of $\max_{x \le x_{tr}} N_{SCF}$ to $\Lambda \geq 30°$ is shown in Figures 16, 17, and 18. Comparing these figures to their $N_{SCF,crit}$ analogues, the present results demonstrate a slightly tighter spread, especially for configurations with lower SCF amplification (e.g., $N < 5$). In sum, this nonlocal metric is a useful and novel alternate visualization for some configurations that experience these mixed-mode, TS/SCF transition pathways.

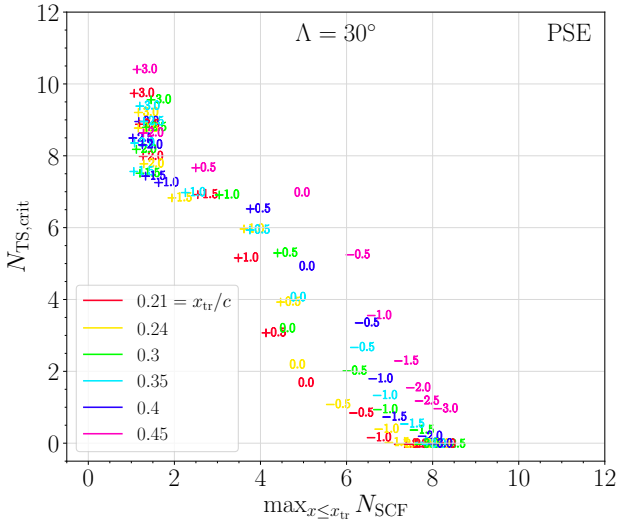

Fig. 16 Continuation of Figure 15 at $\Lambda = 30°$. Compare this with the dual N-factor chart in Figure 11(b).

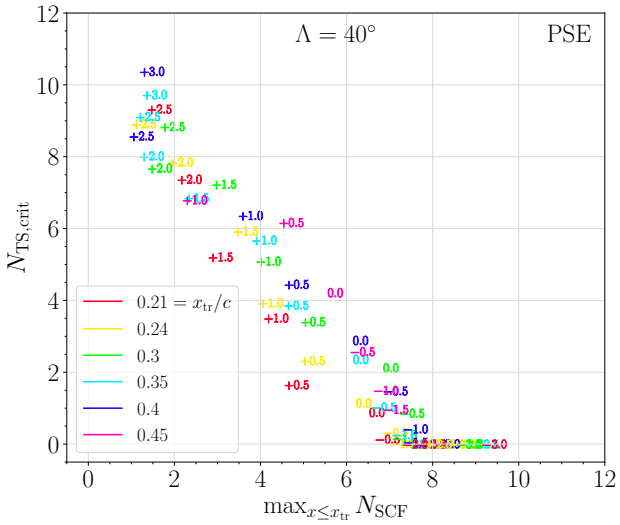

Fig. 17 Continuation of Figure 15 at $\Lambda = 40°$. Compare this with the dual N-factor chart in Figure 12(b).

Acknowledgments

This research is sponsored by the NASA Transformational Tools and Technologies (TTT) project of the Transformative Aeronautics Concepts Program under the Aeronautics Research Mission Directorate. The computational resources supporting this work were provided by the K-cluster at NASA Langley Research Center.

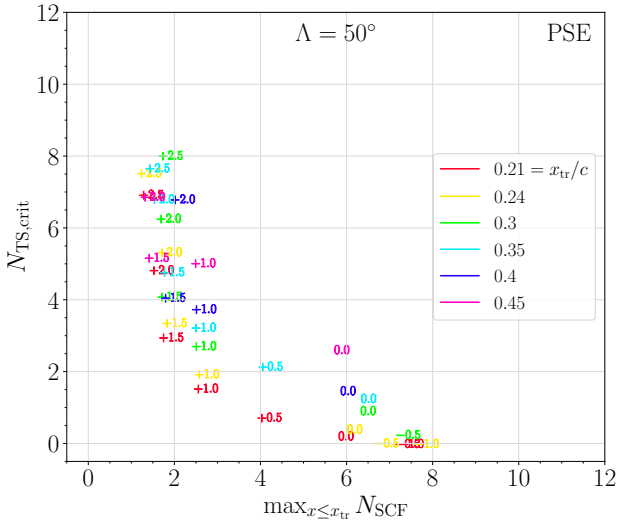

Fig. 18 Continuation of Figure 15 at $\Lambda = 50°$. Compare this with the dual N-factor chart in Figure 13(b).

References

[1] Thibert, J., Reneaux, V., and Schmitt, V., "ONERA Activities in Drag Reduction," *Congress of the International Council of the Aeronautical Sciences, 17th, pp. 1053–64*, 1990.

[2] Joslin, R. D., "Aircraft Laminar Flow Control," *Annual Review of Fluid Mechanics*, Vol. 30, No. 1, 1998, pp. 1–29.

[3] Somers, D. M., "An Exploratory Investigation of a Slotted, Natural-Laminar-Flow Airfoil," NASA CR-2012-217560, 2012.

[4] Morkovin, M., "Transition in Open Flow Systems–a Reassessment," *Bulletin of the American Physical Society*, Vol. 39, 1994, p. 1882.

[5] Arnal, D., "Boundary Layer Transition: Predictions Based on Linear Theory," *Special Course on Progress in Transition Modeling, AGARD 793*, 1994.

[6] Reed, H. L., Saric, W. S., and Arnal, D., "Linear Stability Theory Applied to Boundary Layers," *Annual Review of Fluid Mechanics*, Vol. 28, No. 1, 1996, pp. 389–428.

[7] Schrauf, G., Herbert, T., and Stuckert, G., "Evaluation of Transition in Flight Tests using Nonlinear Parabolized Stability Equation Analysis," *Journal of Aircraft*, Vol. 33, No. 3, 1996, pp. 554–560.

[8] Schrauf, G., "Large-Scale Laminar Flow Tests Evaluated with Linear Stability Theory," AIAA Paper 2001-2444, 2001.

[9] Tufts, M. W., Reed, H. L., Crawford, B. K., Duncan Jr., G. T., and Saric, W. S., "Computational Investigation of Step Excrescence Sensitivity in a Swept-Wing Boundary Layer," *Journal of Aircraft*, Vol. 54, No. 2, 2017, pp. 602–626.

[10] Groot, K. J., Beyak, E. S., Heston, D. T., and Reed, H. L., "Boundary-Layer Stability of a Natural-Laminar-Flow Airfoil at Flight Conditions," AIAA Paper 2020-3052, 2020.

[11] Menter, F. R., Smirnov, P. E., Liu, T., and Avancha, R., "A One-Equation Local Correlation-Based Transition Model," *Flow, Turbulence and Combustion*, Vol. 95, 2015, pp. 583–619.

[12] Leidy, A., Kegerise, M. A., Hannon, J., Choudhari, M. M., Venkatachari, B. S., and Paredes, P., "Measurements and Computations of Natural Transition on the NASA Juncture-Flow Model with a Symmetric Wing," AIAA Paper 2023-0441, 2023.

[13] Slotnick, J. P., Khodadoust, A., Alonso, J., Darmofal, D., Gropp, W., Lurie, E., and Mavriplis, D. J., "CFD Vision 2030 Study: A Path to Revolutionary Computational Aerosciences," NASA CR-2014-218178, 2014.

[14] Boltz, F. W., Kenyon, G. C., and Allen, C. Q., "Effects of Sweep Angle on the Boundary-Layer Stability Characteristics of an Untapered Wing at Low Speeds," NACA TN D-338, 1960.

[15] Venkatachari, B. S., Paredes, P., Choudhari, M. M., Li, F., and Chang, C.-L., "Pretest Computational Assessment of Boundary Layer Transition in the NASA Juncture Flow Model with an NACA 0015-Based Wing," AIAA Paper 2021-2502, 2021.

[16] Hildebrand, N. J., Chang, C.-L., Choudhari, M. M., Li, F., Nielsen, E. J., Venkatachari, B. S., and Paredes, P., "Coupling of the FUN3D Unstructured Flow Solver and the LASTRAC Stability Code to Model Transition," AIAA Paper 2022-1952, 2022.

[17] Venkatachari, B. S., Carnes, J., Chang, C.-L., and Choudhari, M. M., "Boundary-Layer Transition Prediction Through Loose Coupling of OVERFLOW and LASTRAC," AIAA Paper 2022-3682, 2022.

[18] Abbott, I. H., Von Doenhoff, A. E., and Stivers Jr., L., "Summary of Airfoil Data," NACA TR-824, 1945.

[19] Franciolini, M., Da Ronch, A., Drofelnik, J., Raveh, D., and Crivellini, A., "Efficient Infinite-Swept Wing Solver for Steady and Unsteady Compressible Flows," *Aerospace Science and Technology*, Vol. 72, 2018, pp. 217–229.

[20] Krimmelbein, N., "Transition Prediction Method for Three-Dimensional Flows using Linear Stability Theory," Ph.D. thesis, Deutsches Zentrum für Luft- und Raumfahrt Institut für Aerodynamik und Strömungstechnik, 2021.

[21] Derlaga, J. M., Jackson, C. W., and Buning, P. G., "Recent Progress in OVERFLOW Convergence Improvements," AIAA Paper 2020-1045, 2020.

[22] Rumsey, C., "Turbulence Modeling Resource Website," `https://turbmodels.larc.nasa.gov/`, 2023. Accessed: 2023-11-21.

[23] Chan, W., Gomez, R., Rogers, S., and Buning, P., "Best Practices in Overset Grid Generation," AIAA Paper 2002-3191, 2002.

[24] Chan, W. M., Pandya, S. A., Rogers, S. E., Jensen, J. C., Lee, H. C., Kao, D. L., Buning, P. G., Meakin, R. L., Boger, D. A., and Nash, S. M., "Chimera Grid Tools User's Manual," `https://www.nas.nasa.gov/publications/software/docs/chimera/pages/man.html`, 2018. Accessed: 2023-11-22.

[25] Chang, C.-L., "Langley Stability and Transition Analysis Code (LASTRAC) Version 1.2 User Manual," NASA TM-2004-213233, 2004.

[26] Chang, C.-L., "LASTRAC.3d: Transition Prediction in 3D Boundary Layers," AIAA Paper 2004-2545, 2004.

[27] Zhu, Z., Song, W.-P., Han, Z.-H., and Xu, J.-H., "A Comparison Study on Transition Characteristics of NLF Forward-Swept-Wing and Aft-Swept-Wing," Belo Horizonte, Brazil, 2018. 31st Congress of the International Council of the Aeronautical Sciences.

[28] Diakakis, K., Papadakis, G., and Voutsinas, S. G., "Assessment of Transition Modeling for High Reynolds Flows," *Aerospace Science and Technology*, Vol. 85, 2019, pp. 416–428.

[29] Groot, K. J., Beyak, E. S., Heston, D. T., and Reed, H. L., "Boundary-Layer Stability of a Natural-Laminar-Flow Airfoil," AIAA Paper 2020-1024, 2020.

[30] Herbert, T., "Secondary Instability of Boundary Layers," *Annual Review of Fluid Mechanics*, Vol. 20, No. 1, 1988, pp. 487–526.